Langevin Representation of Coulomb Collisions for bi-Maxwellian Plasmas

Petr Hellinger[a,b], Pavel M. Trávníček[a,b,c]

[a] *Astronomical Institute, AS CR, Bocni II/1401, 14131 Prague 4, Czech Republic*
[b] *Institute of Atmospheric Physics, AS CR, Bocni II/1401, 14131 Prague 4, Czech Republic*
[c] *Institute of Geophysics and Planetary Physics, UCLA, Los Angeles, 90095-1567, U.S.A.*

Abstract

Langevin model corresponding to the Fokker-Planck equation for bi-Maxwellian particle distribution functions is developed. Rosenbluth potentials and their derivatives are derived in the form of triple hypergeometric functions. The Langevin model is tested in the case of relaxation of the proton temperature anisotropy and implemented into the hybrid expanding box model. First results of this code are presented and discussed.

Key words: Coulomb collisions, Langevin equation, bi-Maxwellian distribution function, stochastic differential equation

1. Introduction

Coulomb collisions in weakly collisional plasmas are essentially kinetic phenomenon and need a kinetic treatment. In particle-in-cell codes the Coulomb collisions are often modeled by stochastic energy and momentum exchange between randomly paired particles [1–3]. Alternatively, one may use one-particle stochastic forcing given by the Langevin equation corresponding to the Fokker-Planck one; this model was developed for isotropic, Maxwellian scatters [4, 5]. However, weakly collisional plasma often exhibit substantial particle temperature anisotropies (e.g., in the solar wind [6–8]). These observations motivated us to develop a stochastic Langevin model for bi-Maxwellian scatters. A general scheme for any velocity distribution function has been proposed with pending implementation [9]. First, we derive the Rosenbluth potentials in the bi-Maxwellian case (section 2). The model is described in section 3 and is tested on two simple cases of a proton temperature isotropization in section 4. Finally, the collisions are implemented in the framework of the hybrid expanding box and tested in section 5. In section 6 we discuss the presented results.

2. Fokker-Planck Equation and Rosenbluth Potentials

Coulomb collision scattering may be approximated by a Fokker-Planck equation assuming a dominance of two-particle small-angle interactions. The Fokker-Planck equation may be given in the following, Rosenbluth form (for symbol definitions see Appendix B):

$$\left(\frac{\partial f_\mathrm{s}}{\partial t}\right)_\mathrm{coll} = -\sum_\mathrm{t} \frac{q_\mathrm{s}^2 q_\mathrm{t}^2 \ln\Lambda_\mathrm{st}}{4\pi\epsilon_0^2 m_\mathrm{s}^2}\left[\left(1+\frac{m_\mathrm{s}}{m_\mathrm{t}}\right)\frac{\partial}{\partial \boldsymbol{v}}\cdot\left(f_\mathrm{s}\frac{\partial H_\mathrm{t}}{\partial \boldsymbol{v}}\right) - \frac{1}{2}\frac{\partial^2}{\partial \boldsymbol{v}\partial \boldsymbol{v}} : \left(f_\mathrm{s}\frac{\partial^2 G_\mathrm{t}}{\partial \boldsymbol{v}\partial \boldsymbol{v}}\right)\right] \tag{1}$$

where H and G are the Rosenbluth potentials

$$H_\mathrm{s}(\boldsymbol{v}) = \int \frac{f_\mathrm{s}(\boldsymbol{u})}{|\boldsymbol{v}-\boldsymbol{u}|}\mathrm{d}^3u \quad \text{and} \quad G_\mathrm{s}(\boldsymbol{v}) = \int f_\mathrm{s}(\boldsymbol{u})|\boldsymbol{v}-\boldsymbol{u}|\mathrm{d}^3u. \tag{2}$$

For a bi-Maxwellian distribution function

$$f_\mathrm{s} = \frac{n_\mathrm{s}}{(2\pi)^{3/2} v_{\mathrm{s}\parallel} v_{\mathrm{s}\perp}^2}\exp\left(-\frac{v_\perp^2}{2v_{\mathrm{s}\perp}^2} - \frac{v_\parallel^2}{2v_{\mathrm{s}\parallel}^2}\right) \tag{3}$$

one can obtain the following explicit form of the two potentials

$$H_{\rm s} = 4\pi v_{\rm s\perp}^2 f_{\rm s} F\left(\begin{array}{c} 1, \frac{1}{2} \\ \frac{3}{2}; \frac{1}{2} \end{array} , 1 - A_{\rm s}, \frac{A_{\rm s} v_\parallel^2}{2v_{\rm s\parallel}^2}, \frac{v_\perp^2}{2v_{\rm s\perp}^2} \right), \; G_{\rm s} = 8\pi v_{\rm s\perp}^4 f_{\rm s} F\left(\begin{array}{c} 2, \frac{1}{2} \\ \frac{3}{2}; \frac{1}{2} \end{array} , 1 - A_{\rm s}, \frac{A_{\rm s} v_\parallel^2}{2v_{\rm s\parallel}^2}, \frac{v_\perp^2}{2v_{\rm s\perp}^2} \right) \tag{4}$$

where F is a triple hypergeometric function (see Appendix A). For the isotropic (Maxwellian case, $A_{\rm s} = 1$, one recovers the standard results:

$$H_{\rm s} = \frac{n_{\rm s}}{v} {\rm erf}\left(\frac{v}{\sqrt{2} v_{\rm s||}} \right), \quad G_{\rm s} = n_{\rm s} v_{\rm s||} \left[\sqrt{\frac{2}{\pi}} {\rm e}^{-\frac{v^2}{2v_{\rm s||}^2}} + \left(\frac{v_{\rm s||}}{v} + \frac{v}{v_{\rm s||}} \right) {\rm erf}\left(\frac{v}{\sqrt{2} v_{\rm s||}} \right) \right]. \tag{5}$$

3. Langevin equation

The collisional diffusion in the velocity space is equivalent to a stochastic forcing [4]. Let us for simplicity assume only one species and only interspecies collisions. We have the Fokker-Planck equation

$$\left(\frac{\partial f_{\rm s}}{\partial t} \right)_{\rm coll} = -\frac{\partial}{\partial \boldsymbol{v}} \cdot (\boldsymbol{a}_{\rm s} f_{\rm s}) + \frac{\partial^2}{\partial \boldsymbol{v} \partial \boldsymbol{v}} : (\mathbf{D}_{\rm s} f_{\rm s}) \tag{6}$$

with the acceleration

$$\boldsymbol{a}_{\rm s} = \frac{q_{\rm s}^4 \ln \Lambda_{\rm ss}}{2\pi \epsilon_0^2 m_{\rm s}^2} \frac{\partial H_{\rm s}}{\partial \boldsymbol{v}} \tag{7}$$

and the diffusion matrix

$$\mathbf{D}_{\rm s} = \frac{q_{\rm s}^4 \ln \Lambda_{\rm ss}}{8\pi \epsilon_0^2 m_{\rm s}^2} \frac{\partial^2 G_{\rm s}}{\partial \boldsymbol{v} \partial \boldsymbol{v}} \tag{8}$$

The Fokker-Planck equation (6) is equivalent to the Langevin equation in the finite difference form

$$\Delta \boldsymbol{v} = \boldsymbol{a}_{\rm s} \Delta t + \boldsymbol{Q} \tag{9}$$

where $\boldsymbol{Q}$ is a random vector with the probability [4]

$$\phi(\boldsymbol{Q}) = \frac{1}{(2\pi \Delta t)^{3/2} \sqrt{\det \mathbf{D}_{\rm s}}} \exp\left(-\frac{\boldsymbol{Q} \cdot \mathbf{D}_{\rm s}^{-1} \cdot \boldsymbol{Q}}{2\Delta t} \right) \tag{10}$$

where $\mathbf{D}_{\rm s}^{-1}$ is the inverse matrix of $\mathbf{D}_{\rm s}$. For a Maxwellian distribution function it is simple to generate the random vector $\boldsymbol{Q}$ taking a coordinate system where $\boldsymbol{v} = (0, 0, v)$ and where $\mathbf{D}_{\rm s}$ is diagonal [4]. In the bi-Maxwellian case one can assume coordinates where $\boldsymbol{v} = (v_x, v_y, v_z) = (v_\perp, 0, v_\parallel)$. In these coordinates it is easy to calculate $\partial H_{\rm s}/\partial \boldsymbol{v}$ needed for acceleration:

$$\frac{\partial H_{\rm s}}{\partial v_x} = -\frac{4}{3}\pi v_\perp f_{\rm s} F\left(\begin{array}{c} 1, \frac{1}{2} \\ \frac{5}{2}; \frac{1}{2} \end{array} \right), \quad \frac{\partial H_{\rm s}}{\partial v_y} = 0, \quad \frac{\partial H_{\rm s}}{\partial v_z} = -\frac{4}{3}\pi A_{\rm s} v_\parallel f_{\rm s} F\left(\begin{array}{c} 1, \frac{3}{2} \\ \frac{5}{2}; \frac{3}{2} \end{array} \right). \tag{11}$$

For the diffusion matrix we need to calculate $\partial^2 G_{\rm s}/\partial \boldsymbol{v} \partial \boldsymbol{v}$ which may be given as

$$\begin{aligned}
\frac{\partial^2 G_{\rm s}}{\partial v_x^2} &= \frac{8}{3}\pi v_{\rm s\perp}^2 f_{\rm s} \left[F\left(\begin{array}{c} 2, \frac{1}{2} \\ \frac{5}{2}; \frac{1}{2} \end{array} \right) - \frac{1}{5} \frac{v_\perp^2}{v_{\rm s\perp}^2} F\left(\begin{array}{c} 2, \frac{1}{2} \\ \frac{7}{2}; \frac{1}{2} \end{array} \right) \right] \\
\frac{\partial^2 G_{\rm s}}{\partial v_y^2} &= \frac{8}{3}\pi v_{\rm s\perp}^2 f_{\rm s} F\left(\begin{array}{c} 2, \frac{1}{2} \\ \frac{5}{2}; \frac{1}{2} \end{array} \right) \\
\frac{\partial^2 G_{\rm s}}{\partial v_z^2} &= \frac{8}{3}\pi A_{\rm s} v_{\rm s\perp}^2 f_{\rm s} \left[F\left(\begin{array}{c} 2, \frac{3}{2} \\ \frac{5}{2}; \frac{3}{2} \end{array} \right) - \frac{1}{5} \frac{v_\parallel^2}{v_{\rm s\parallel}^2} F\left(\begin{array}{c} 2, \frac{5}{2} \\ \frac{7}{2}; \frac{5}{2} \end{array} \right) \right] \\
\frac{\partial^2 G_{\rm s}}{\partial v_z \partial v_x} &= -\frac{8}{15}\pi A_{\rm s} v_\perp v_\parallel f_{\rm s} F\left(\begin{array}{c} 2, \frac{3}{2} \\ \frac{7}{2}; \frac{3}{2} \end{array} \right) \\
\frac{\partial^2 G_{\rm s}}{\partial v_z \partial v_y} &= \frac{\partial^2 G_{\rm s}}{\partial v_x \partial v_y} = 0.
\end{aligned} \tag{12}$$

Note that in the above expressions, Eqs. (11,12), we have dropped the argument $1-A_\mathrm{s}$, $A_\mathrm{s}v_\parallel^2/2v_{\mathrm{s}\parallel}^2$, $v_\perp^2/2v_{\mathrm{s}\perp}^2$ of F. The diffusion term $\partial^2 G_\mathrm{s}/\partial\boldsymbol{v}\partial\boldsymbol{v}$ is not diagonal and needs to be diagonalized but only in the two dimensional x-z plane which is trivial. Then one gets a diagonalized diffusion matrix $\mathbf{D}_\mathrm{s}$ and one can easily generate the random quantity $\boldsymbol{Q}$ [4].

4. Numerical tests

To test the Langevin model we consider only one population of protons (henceforth we will drop the proton index when not necessary) with an initial bi-Maxwellian distribution function. The result of the Langevin model will be compared with the predicted isotropization rate by proton-proton collisions: the isotropization frequency ν_T [10],

$$\left(\frac{\mathrm{d}T_\perp}{\mathrm{d}t}\right)_\mathrm{coll} = -\frac{1}{2}\left(\frac{\mathrm{d}T_\parallel}{\mathrm{d}t}\right)_\mathrm{coll} = -\nu_T\left(T_\perp - T_\parallel\right) \tag{13}$$

may be given as [11]

$$\nu_T = \frac{e^4 n \ln\Lambda}{30\pi^{3/2}\epsilon_0^2 m_\mathrm{p}^2 v_{\mathrm{p}\parallel}^3}\ {}_2F_1\left(\begin{array}{c} 2, 3/2 \\ 7/2 \end{array}, 1-\frac{T_\perp}{T_\parallel}\right) \tag{14}$$

where ${}_2F_1$ is the standard (Gauss) hypergeometric function.

First we start with protons having $T_\perp = 4T_\parallel$. We use 500,000 macroparticles representing the proton distribution function. Each time step parallel and perpendicular thermal velocities are calculated from the macroparticles as second order moments. Then, particle velocities are advanced by the random force, Eq. (9), which is calculated for each particles using the calculated moments; Evaluating the triple hypergeometric function F (we use its integral representation, Eq. (18)) for derivatives of H and G for each particle is impractical; instead, we evaluate F on a 256×256 grid (for each set of parameters) in the velocity space $(v_\parallel, v_\perp)$ and for each particle we interpolate the function values from this grid (the hypergeometric functions are very smooth and we have tested that this method introduces only minimum differences between the real and interpolated values). We use a small time step $\Delta t = 10^{-4}\nu_{T0}^{-1}$ where ν_{T0} is the initial value of the isotropization frequency, Eq. (14).

Figure 1 shows the results of the Langevin model: the solid line denotes the proton temperature anisotropy $T_\perp/T_\parallel$ as a function of time t whereas the dotted line shows the predicted evolution of $T_\perp/T_\parallel$ obtained by integration of Eq. (13) [12]. The Langevin model initially exhibits very good agreement with the theoretical prediction based on Eq. (13). During the collisional evolution the distribution function slightly departs from a bi-Maxwellian shape and therefore its evolution is not governed by Eq. (13) derived assuming the distribution function is exactly bi-Maxwellian. At the same time the Langevin model based on the bi-Maxwellian velocity distribution function is strictly speaking no longer valid as well. The extend of these departures is shown in Figure 2 which shows the evolution of the third moments of the velocity distribution function (left) $\int v_\perp^3 f\mathrm{d}^3v$ and (right) $\int |v_\parallel|^3 f\mathrm{d}^3v$ normalized to the bi-Maxwellian predictions $3(\pi/2)^{1/2}nv_{\mathrm{p}\perp}^3$ and $4nv_{\mathrm{p}\parallel}^3/(2\pi)^{1/2}$ (where $v_{\mathrm{p}\perp}^2 = \int v_\perp^2 f\mathrm{d}^3v/(2n)$ and $v_{\mathrm{p}\parallel}^2 = \int v_\parallel^2 f\mathrm{d}^3v/(n)$). These departures from the bi-Maxwellian shape results from the strong velocity dependent property of the Coulomb collisions. The less energetic, core protons thermalize faster while the more energetic protons thermalize slower. This effect generates an excess of the protons with larger perpendicular velocities leading to larger perpendicular moment $\int v_\perp^3 f\mathrm{d}^3v$ (as well as to smaller parallel moment $\int |v_\parallel|^3 f\mathrm{d}^3v$) compared to the bi-Maxwellian expectations. At later times the velocity distibution function thermalizes and the moments approach the Maxwellian predictions.

For the next test we use the opposite initial temperature anisotropy $T_\parallel = 4T_\perp$. All the other parameters of the model are the same as in the previous test. Figure 3 shows the results of the Langevin model in second case: the solid line denotes the proton temperature anisotropy $T_\parallel/T_\perp$ as a function of time t whereas the dotted line shows the predicted evolution of $T_\perp/T_\parallel$ obtained by integration of Eq. (13). Again the Langevin model exhibit initially a very good agreement with the theoretical prediction based on Eq. (13). Later time deviation from this predicted evolution is caused by departures of the proton distribution function from

a bi-Maxwellian shape as in the previous case. Figure 4 shows the evolution of the third moments of the velocity distribution function (left) $\int v_\perp^3 f \mathrm{d}^3 v$ and (right) $\int |v_\parallel|^3 f \mathrm{d}^3 v$ normalized to the bi-Maxwellian predictions $3(\pi/2)^{1/2} n v_{\mathrm{p}\perp}^3$ and $4 n v_{\mathrm{p}\parallel}^3/(2\pi)^{1/2}$. In this case of the opposite anisotropy the velocity dependent Coulomb collisions generate an excess of the protons with larger parallel velocities leading to larger parallel moment $\int |v_\parallel|^3 f \mathrm{d}^3 v$ (as well as to smaller perpendicular moment $\int v_\perp^3 f \mathrm{d}^3 v$) compared to the bi-Maxwellian expectations. At later times the velocity distibution function thermalizes and the moments approach the Maxwellian predictions.

5. Collisions in expanding box

In the previous tests the system started with anisotropic protons and than relaxed towards isotropy. In the solar wind the expansion drives the temperature anisotropy continuously [13]. To study the response of the plasma to a slow expansion one can use the expanding box model implemented in the hybrid code [14, 15]. The expanding box simulations can model both the anisotropy formation from expansion and its relaxation via collisions and kinetic instabilities. In the present Collisional Hybrid Expanding Box (CHEB) model the expansion is described as an external force. One assumes a solar wind with a constant radial velocity U at a radial distance R. Transverse scales (with respect to the radial direction) of a small portion of plasma, co-moving with the solar wind velocity, increase with time $y, z \propto (1 + t/t_e) y, z$ where $t_e = R/U$ is a characteristic time of the expansion. The expanding box uses these co-moving coordinates, the physical transverse scales of the simulation box increase with time [15]. Coulomb collision are included by the Langevin stochastic random force.

The characteristic spatial and temporal units used in the model are c/ω_{pp0} and $1/\omega_{\mathrm{cp}0}$ respectively, We use the spatial resolution $\Delta x = \Delta y/2 = 2c/\omega_{pp0}$, and there are $1,024$ particles per cell. Fields and moments are defined on a 2-D periodic x–y grid with dimensions 256×256. Protons are advances using the Boris' scheme with a time step $\Delta t = 0.05/\omega_{\mathrm{cp}0}$, while the magnetic field $\boldsymbol{B}$ is advanced with a smaller time step $\Delta t_B = \Delta t/10$. The initial ambient magnetic field is directed along the radial, x direction, $\boldsymbol{B}_0 = (B_0, 0, 0)$, and we impose a continuous expansion in y and z directions with a characteristic time $t_e = 10^4/\omega_{\mathrm{cp}0}$. For the strictly radial magnetic field the expansion leads to a decrease of the ambient density and magnitude of the magnetic field as $n, B \propto (1 + t/t_e)^{-2}$. Collisional stochastic forcing through the Langevin equation is performed each 10 time steps; the initial isotropization frequency ν_{T0} is chosen to be $\nu_{T0} t_e = 1/4$. Protons are initialized with a bi-Maxwellian distribution function with $T_\perp/T_\parallel = 0.4$ and $\beta_\parallel = 0.3$.

Without collisions the system would evolve in the doubly adiabatic manner (heat fluxes are neglected in the model as a spatial homogeneity is assumed)

$$\left(\frac{\mathrm{d}T_\parallel}{\mathrm{d}t}\right)_{\mathrm{CGL}} = 2\frac{T_\parallel}{n}\frac{\mathrm{d}n}{\mathrm{d}t} - 2\frac{T_\parallel}{B}\frac{\mathrm{d}B}{\mathrm{d}t} \quad \text{and} \quad \left(\frac{\mathrm{d}T_\perp}{\mathrm{d}t}\right)_{\mathrm{CGL}} = \frac{T_\perp}{B}\frac{\mathrm{d}B}{\mathrm{d}t} \tag{15}$$

if there are no wave activity [16]. When Coulomb collisions are present (and heat fluxes are negligible) one gets a theoretical prediction for the evolution of the two temperatures by coupling Eqs. (13,15), i.e., taking $\mathrm{d}/\mathrm{d}t = (\mathrm{d}/\mathrm{d}t)_{\mathrm{CGL}} + (\mathrm{d}/\mathrm{d}t)_{\mathrm{coll}}$.

The evolution of the proton temperature anisotropy in the 2-D CHEB simulation with proton-proton collisions is shown in Figure 5. The solid line shows the proton temperature anisotropy $T_\perp/T_\parallel$ as a function of time while the dotted line displays the collisional prediction (coupled model of Eqs. (13,15)). As in the static case in the previous section the CHEB model results is in a good agreement with the collisional prediction during an initial phase. Later on the model departs from the prediction, first weakly then quite strongly; $T_\perp/T_\parallel$ exhibits pronounced oscillations at later times. A natural suspect cause for such a behavior is a kinetic instability driven by the temperature anisotropy. To verify the role of possible temperature-anisotropy driven instability it is useful to display the evolution as a path in the space of the proton parallel beta $\beta_\parallel$ and the proton temperature anisotropy $T_\perp/T_\parallel$) which are dominant parameters for electromagnetic instabilities [16]. This is done in Fig. 6 showing the path by solid curves in the two panels (the empty circles denote the initial conditions). The dashed contours show the linear prediction in a homogeneous plasma with bi-Maxwellian protons, the maximum growth rate γ_m (in units of ω_{cp}) as a function of $\beta_\parallel$ and $T_\perp/T_\parallel$

for the parallel proton fire hose (left panel) and the oblique one (right panel). The dotted lines display the collisional prediction whereas the dash-dotted lines show the collisionless double adiabatic predictions (Eq. (15)).

The evolution of the weakly collisional expansion exhibit oscillations in the space $(\beta_\parallel, T_\perp/T_\parallel)$. During the initial phase, the system follows the collisional prediction given by the coupled system of Eqs. (13,15). Around the first crossing of the $\gamma_m = 10^{-3}\omega_{cp}$ contour of the parallel fire hose (Figure 6, left panel) the system starts to deviated from the prediction partly because of collisionally induced departures from bi-Maxwellian shape (see previous section) and partly because of development of the parallel fire hose instability which becomes the dominant phenomenon as the system gets relatively far into the nominally instable region [17]. The system eventually enters the unstable region with respect to the oblique fire hose and consequently it rapidly jumps back to the region stable to with respect to the oblique fire hose owing to the special self-destructing nonlinear behavior of the oblique instability [16]. This phase starts close to the first crossing of the $\gamma_{\rm m} = 10^{-3}\omega_{\rm cp}$ contour of the oblique fire hose (Figure 6, right panel). Afterwards, the system oscillates between the unstable and stable regions (with respect to the oblique fire hose) with smaller variations of the temperature anisotropy $T_\perp/T_\parallel$ The later evolution of the weakly collisional system is dominated by instabilities similarly as in the collisionless system [16].

The interaction between protons and instability generated waves is resonant through normal and anomalous cyclotron resonances [16]. The proton velocity distribution function is mainly affected at the resonances. Figure 7 shows contour plots of the proton distribution function $f(v_\parallel, v_\perp)$ at (left) $t = 0.4/\nu_{T0}$ and (right) at the end of the simulations. Velocities are given in units of the Alfvén velocity $v_A = B_0/(\mu_0 m_{\rm p} n)^{1/2}$ Figure 7 (left panel) shows the result of the interaction between protons and the parallel fire hose driven ion whistler waves: affected are mainly particles with high parallel velocities $|v_\parallel| \sim 2v_A$ which are required for the anomalous cyclotron resonance [17]. Figure 7 (right panel) shows mainly the effect of the proton scattering by the oblique fire hose driven Alfvén waves interacting through the (normal) cyclotron resonance [16]. This scattering affects strongly particles with $|v_\parallel| \sim v_A$. The wave-particle interaction leads to departures of the velocity distribution function and the bi-Maxwellian Langevin model is strictly speaking no longer valid.

6. Conclusions

Rosenbluth potentials for bi-Maxwellian particle distribution function (in the form of triple hypergeometric functions) are derived and Langevin model corresponding to the Fokker-Planck collision term in bi-Maxwellian plasmas is developed, generalizing the isotropic case [4]. The Langevin stochastic forcing was tested on simple case of proton temperature isotropization showing a good agreement between the model and predictions based on bi-Maxwellian transport coefficients when the distribution functions are close to bi-Maxwellian. The collisional stochastic forcing was implemented into the hybrid expanding box model. First results of this code show that in a (sufficiently) weakly collisional plasma Coulomb collisions are unable to stop the proton temperature anisotropy driven by the expansion so that kinetic instabilities arise and bound the proton temperature anisotropy.

Coulomb collisions as well as wave-particle interactions lead to departures of the velocity distribution function from the bi-Maxwellian shape. Consequently, the bi-Maxwellian Langenvin model is strictly speaking no longer valid. We expect that the model is an acceptable approximation of the Fokker-Plank model approximation [18] as long as the velocity distribution function remains close to bi-Maxwellian shape (or to a superposion of bi-Maxwellian velocity distribution functions [4]). The level of approximation for a given distribution function is, however, an open problem needing a comparison of the model predictions with the results of the Fokker-Plank equation or with the general scheme [9]. The presented bi-Maxwellian Langevin model is more appropriate for anisotropic plasmas but is more complex and more computationally demanding compared to the isotropic model.

Acknowledgements

This work was supported by the Czech grants GAAV IAA300420702 and IAA300420602. Authors acknowledge the computer algebra system Maxima. The CHEB simulation was performed on Amalka super-

computing facility at IAP, ASCR.

A. Triple hypergeometric function

F is a special case of the triple hypergeometric function [19] defined as

$$F\left(\begin{array}{c} a,b \\ c;d \end{array},x,y,z\right)=\sum_{k,l,m=0}^{\infty}\frac{(a)_{k+l+m}(b)_{k+l}}{(c)_{k+l+m}(d)_l}\frac{x^k}{k!}\frac{y^l}{l!}\frac{z^m}{m!} \tag{16}$$

where, $(a)_n$ is a Pochhammer symbol

$$(a)_n=\frac{\Gamma(a+n)}{\Gamma(a)}=a(a+1)\dots(a+n-1). \tag{17}$$

For $b=d$ one can get the simple integral representation

$$F\left(\begin{array}{c} a,b \\ c;b \end{array},x,y,z\right)=\frac{\Gamma(c)}{\Gamma(a)\Gamma(c-a)}\int_0^1\frac{\tau^{a-1}(1-\tau)^{c-a-1}}{(1-\tau x)^b}\exp\left(\frac{\tau y}{1-\tau x}+\tau z\right)\mathrm{d}\tau. \tag{18}$$

The derivation of Eq. (18) is analogous to that of the integral representation of the standard hypergeometric function [11, 20].

The triple hypergeometric function F has these useful recurrence properties

$$\frac{a}{c}F\left(\begin{array}{c} a+1,b \\ c+1;d \end{array},x,y,z\right)-F\left(\begin{array}{c} a,b \\ c;d \end{array},x,y,z\right) = \frac{a-c}{c}F\left(\begin{array}{c} a,b \\ c+1;d \end{array},x,y,z\right) \tag{19}$$

$$F\left(\begin{array}{c} a,b+1 \\ c;b+1 \end{array},x,y,z\right)-F\left(\begin{array}{c} a,b \\ c,b \end{array},x,y,z\right) = \frac{ax}{c}F\left(\begin{array}{c} a+1,b+1 \\ c+1;b+1 \end{array},x,y,z\right). \tag{20}$$

B. Glossary

Here $\perp$ and $\parallel$ denote the directions with respect to the ambient magnetic field $\boldsymbol{B}_0$, $B_0=|\boldsymbol{B}_0|$ denotes its the magnitude; $\boldsymbol{v}$ (and $\boldsymbol{u}$) denotes a velocity, $v=|\boldsymbol{v}|$ being its magnitude, and $v_\parallel$ and $v_\perp$ denote magnitude of the velocity components parallel and perpendicular to $\boldsymbol{B}_0$, respectively; t denotes the time. Here subscripts s (and t) denotes different species; p (or nothing) stands for protons; subscript 0 denotes the intial value. Here f_s denotes the velocity distribution function, and $T_{\mathrm{s}\perp}$ and $T_{\mathrm{s}\parallel}$ denote the perpendicular and parallel temperatures, respectively; $A_\mathrm{s}=T_{\mathrm{s}\perp}/T_{\mathrm{s}\parallel}$ is the temperature anisotropy and $\beta_{\mathrm{s}\parallel}=2\mu_0 n_\mathrm{s}k_B T_{\mathrm{s}\parallel}/B_0^2$ are is the parallel beta. Here $\omega_{c\mathrm{s}}=q_\mathrm{s}B_0/m_\mathrm{s}$ and $\omega_{p\mathrm{s}}=(n_\mathrm{s}q_\mathrm{s}^2/m_\mathrm{s}\epsilon_0)^{1/2}$ denote the cyclotron and plasma frequencies, respectively, $v_{\mathrm{s}\parallel}=(k_BT_{\mathrm{s}\parallel}/m_\mathrm{s})^{1/2}$ and $v_{\mathrm{s}\perp}=(k_BT_{\mathrm{s}\perp}/m_\mathrm{s})^{1/2}$ denote the parallel and perpendicular thermal velocity, respectively. In these expressions m_s, q_s, and n_s denote the mass, the charge, and the number density, respectively (the proton charge is $q_\mathrm{p}=e$); ϵ_0 and μ_0 denote the vacuum electric permittivity and magnetic permeability, respectively; k_B is Boltzmann constant. Here $\ln\Lambda_\mathrm{st}$ stands for the Coulomb logarithm and Γ is the standard Gamma function.

References

[1] T. Takizuka, H. Abe, A binary collision model for plasma simulation with a particle code, J. Comput. Phys. 25 (1977) 205–219.

[2] K. Nanbu, Theory of cumulative small-angle collisions in plasmas, Phys. Rev. E 55 (1997) 4642–4652.

[3] A. M. Dimits, C. Wang, R. Caflisch, B. I. Cohen, Y. Huang, Understanding the accuracy of Nanbu's numerical Coulomb collision operator, J. Comput. Phys. 228 (2009) 4881–4892.

[4] W. M. Manheimer, M. Lampe, G. Joyce, Langevin representation of Coulomb collisions in PIC simulations, J. Comput. Phys. 138 (1997) 563–584.

[5] D. S. Lemons, D. Winske, W. Daughton, B. Albright, Small-angle Coulomb collision model for particle-in-cell simulations, J. Comput. Phys. 228 (2009) 1391–1403.
[6] P. Hellinger, P. Trávníček, J. C. Kasper, A. J. Lazarus, Solar wind proton temperature anisotropy: Linear theory and WIND/SWE observations, Geophys. Res. Lett. 33. doi:10.1029/2006GL025925.
[7] Š. Štverák, P. Trávníček, M. Maksimovic, E. Marsch, A. Fazakerley, E. E. Scime, Electron temperature anisotropy constraints in the solar wind, J. Geophys. Res. 113. doi:10.1029/2007JA012733.
[8] J. C. Kasper, A. J. Lazarus, S. P. Gary, Hot solar-wind helium: Direct evidence for local heating by Alfvén-cyclotron dissipation, Phys. Rev. Lett. 101.
[9] F. L. Hinton, Simulating Coulomb collisions in a magnetized plasma, Phys. Plasmas 15 (2008) 042501.
[10] V. I. Kogan, The rate of equalization of the temperatures of charged particles in a plasma, in: M. A. Leontovich (Ed.), Plasma Physics and the Problem of Controlled Thermonuclear Reactions, Vol. 1, Pergamon Press, New York, 1961, pp. 153–161.
[11] P. Hellinger, P. M. Trávníček, On Coulomb collisions in bi-Maxwellian plasmas, Phys. Plasmas 16 (2009) 054501.
[12] H. Schamel, H. Hamnén, D. F. Düchs, T. E. Stringer, M. R. O'Brien, Nonlinear analysis of Coulomb relaxation of anisotropic distributions, Phys. Fluids B 1 (1989) 76–86.
[13] L. Matteini, S. Landi, P. Hellinger, F. Pantellini, M. Maksimovic, M. Velli, B. E. Goldstein, E. Marsch, The evolution of the solar wind proton temperature anisotropy from 0.3 to 2 AU, Geophys. Res. Lett. 34. doi:10.1029/2007GL030920.
[14] A. Matthews, Current advance method and cyclic leapfrog for 2D multispecies hybrid plasma simulations, J. Comput. Phys. 112 (1994) 102–116.
[15] P. Hellinger, P. Trávníček, Magnetosheath compression: Role of characteristic compression time, alpha particle abundances and alpha/proton relative velocity, J. Geophys. Res. 110. doi:10.1029/2004JA010687.
[16] P. Hellinger, P. M. Trávníček, Oblique proton fire hose instability in the expanding solar wind: Hybrid simulations, J. Geophys. Res. 113. doi:10.1029/2008JA013416.
[17] L. Matteini, S. Landi, P. Hellinger, M. Velli, Parallel proton fire hose instability in the expanding solar wind: Hybrid simulations, J. Geophys. Res. 111. doi:10.1029/2006JA011667.
[18] E. C. Shoub, Failure of the Fokker-Planck approximation to the Boltzmann integral for (1/r) potentials, Phys. Fluids 30 (1987) 1340–1352.
[19] H. Exton, Multiple hypergeometric functions and applications, Mathematics & its Applications, Halsted Press, New York, 1976.
[20] N. N. Lebedev, Special Functions and Their Applications, Prentice-Hall, Inc., Englewood Clifs, N. J., 1965.

Figure Captions

Figure 1. Proton temperature anisotropy $T_\perp/T_\parallel$ as a function of time t (solid line). Dotted line shows the predicted evolution of $T_\perp/T_\parallel$ obtained by integration of Eq. (13).

Figure 2. Evolution of the third moments of the velocity distribution function (left) $\int v_\perp^3 f \mathrm{d}^3v$ and (right) $\int |v_\parallel|^3 f \mathrm{d}^3v$ normalized to the bi-Maxwellian predictions $3(\pi/2)^{1/2} n v_{\mathrm{p}\perp}^3$ and $4nv_{\mathrm{p}\parallel}^3/(2\pi)^{1/2}$, respectively.

Figure 3. Proton temperature anisotropy $T_\parallel/T_\perp$ as a function of time t (solid line). Dotted line shows the predicted evolution of $T_\parallel/T_\perp$ obtained by integration of Eq. (13).

Figure 4. Evolution of the third moments of the velocity distribution function (left) $\int v_\perp^3 f \mathrm{d}^3v$ and (right) $\int |v_\parallel|^3 f \mathrm{d}^3v$ normalized to the bi-Maxwellian predictions $3(\pi/2)^{1/2} n v_{\mathrm{p}\perp}^3$ and $4nv_{\mathrm{p}\parallel}^3/(2\pi)^{1/2}$, respectively.

Figure 5. Evolution in the 2-D CHEB simulation: Proton temperature anisotropy $T_\perp/T_\parallel$ as a function of time. The dotted line displays the collisional prediction.

Figure 6. Evolution in the 2-D CHEB simulation: Path in the space $(\beta_\parallel, T_\perp/T_\parallel)$ is shown by solid curves; the empty circles denote the initial conditions whereas the full circles denotes the end of a first oscillation. The dashed contours shows the linear prediction in a homogeneous plasma with bi-Maxwellian protons, the maximum growth rate (in units of ω_{cp}) as a function of $\beta_\parallel$ and $T_\perp/T_\parallel$ for (left) the parallel proton fire hose and (right) the oblique one. The dotted lines display the collisional prediction whereas the dash-dotted lines show the collisionless, double adiabatic prediction.

Figure 7. Contour plots of the proton distribution function $f(v_\parallel, v_\perp)$ at (left) $t = 0.4/\nu_{T0}$ and (right) at the and of the simulations.

Figures

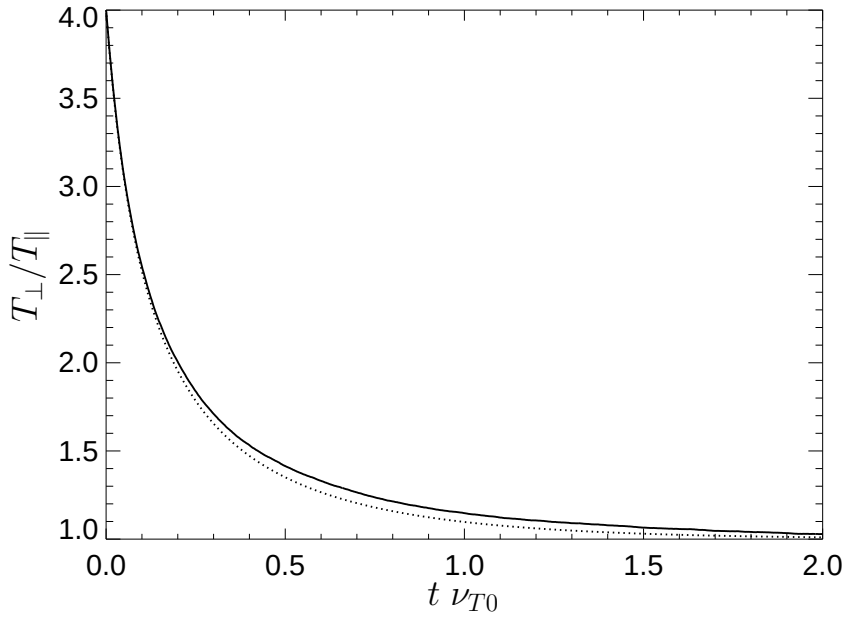

Figure 1: Proton temperature anisotropy $T_\perp/T_\parallel$ as a function of time t (solid line). Dotted line shows the predicted evolution of $T_\perp/T_\parallel$ obtained by integration of Eq. (13).

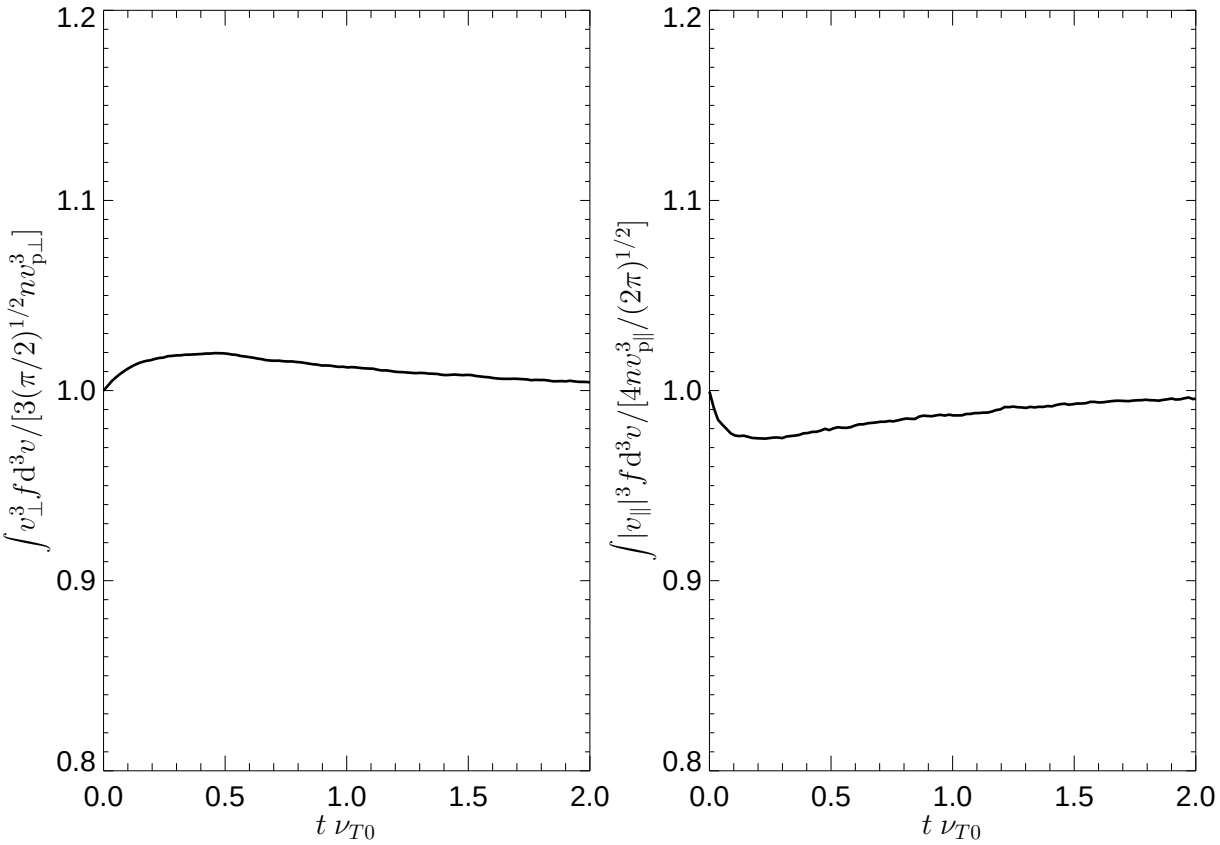

Figure 2: Evolution of the third moments of the velocity distribution function (left) $\int v_\perp^3 f \mathrm{d}^3v$ and (right) $\int |v_\parallel|^3 f \mathrm{d}^3v$ normalized to the bi-Maxwellian predictions $3(\pi/2)^{1/2} n v_{\mathrm{p}\perp}^3$ and $4n v_{\mathrm{p}\parallel}^3/(2\pi)^{1/2}$, respectively.

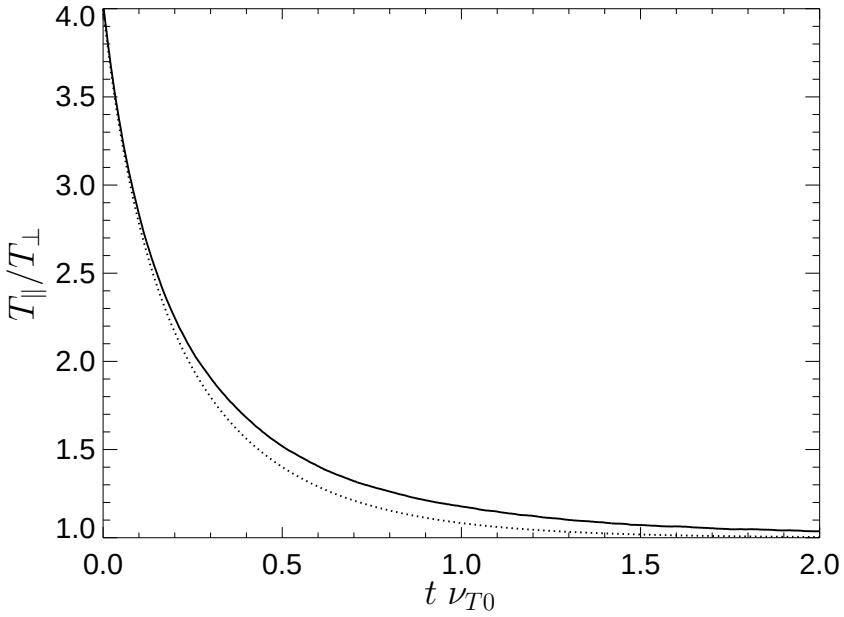

Figure 3: Proton temperature anisotropy $T_\parallel/T_\perp$ as a function of time t (solid line). Dotted line shows the predicted evolution of $T_\parallel/T_\perp$ obtained by integration of Eq. (13).

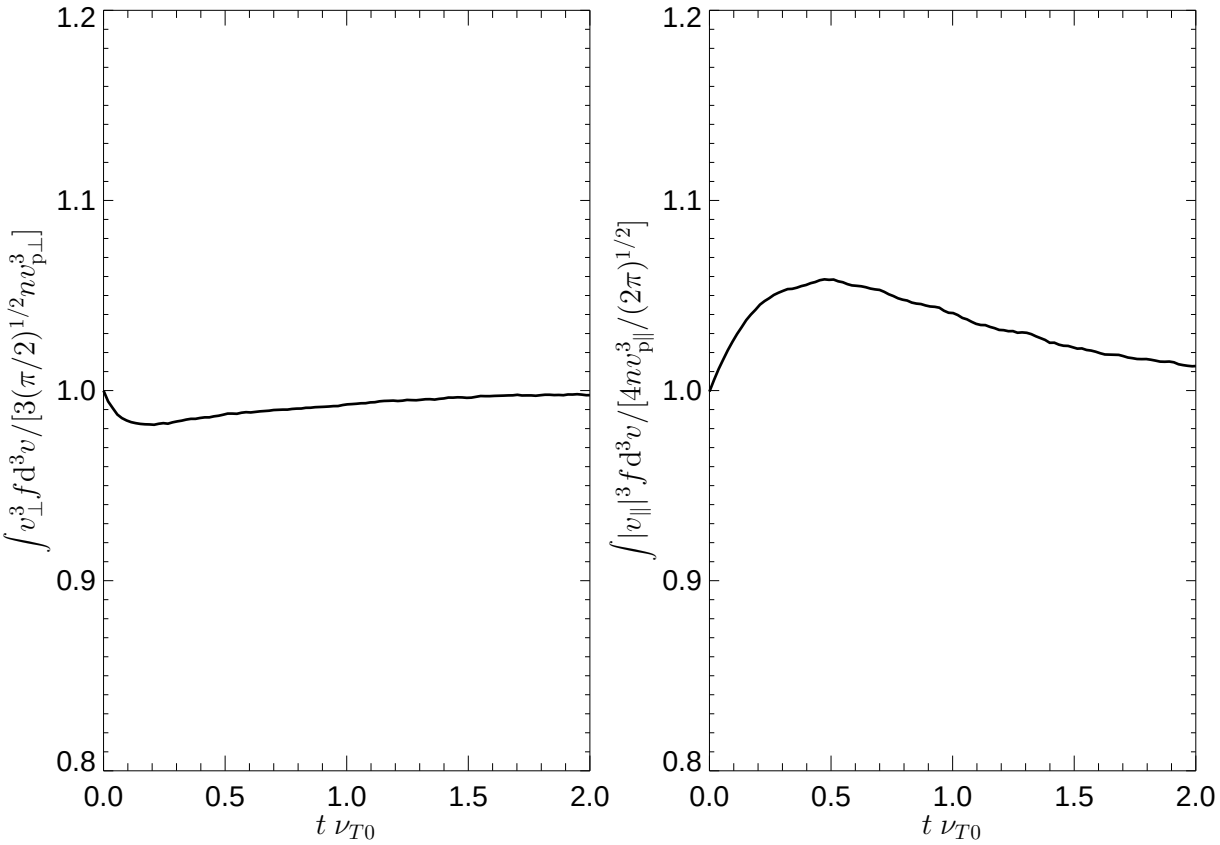

Figure 4: Evolution of the third moments of the velocity distribution function (left) $\int v_\perp^3 f \mathrm{d}^3v$ and (right) $\int |v_\parallel|^3 f \mathrm{d}^3v$ normalized to the bi-Maxwellian predictions $3(\pi/2)^{1/2} n v_{\mathrm{p}\perp}^3$ and $4n v_{\mathrm{p}\parallel}^3/(2\pi)^{1/2}$, respectively.

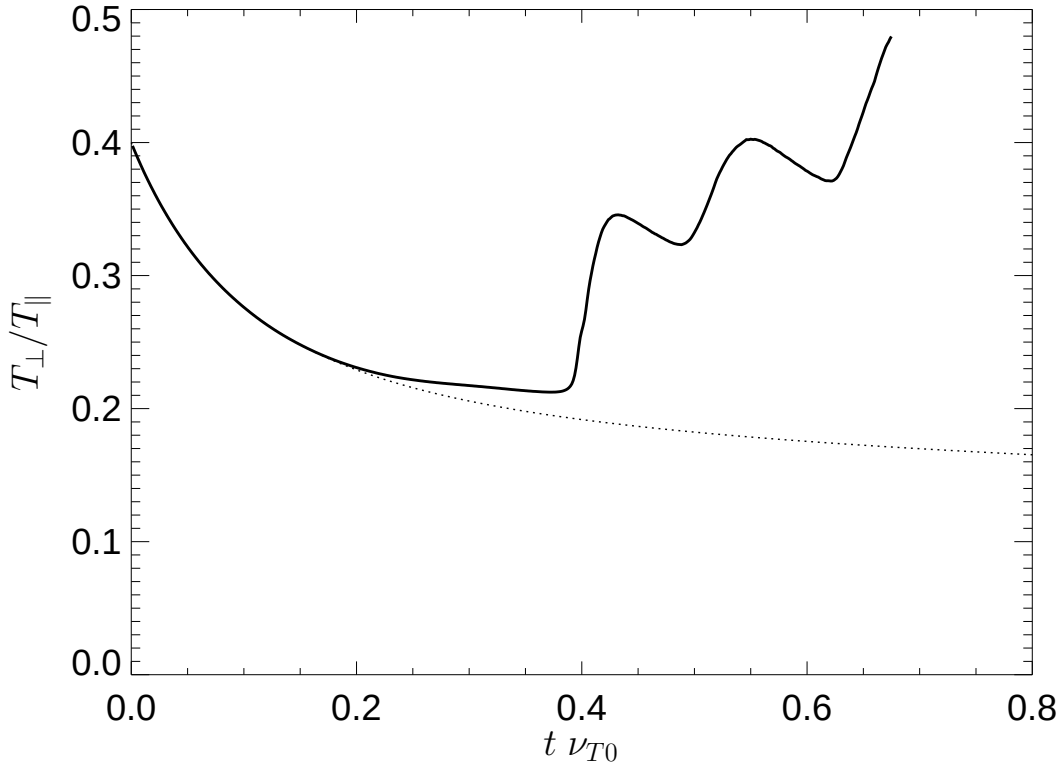

Figure 5: Evolution in the 2-D CHEB simulation: Proton temperature anisotropy $T_\perp/T_\parallel$ as a function of time. The dotted line displays the collisional prediction.

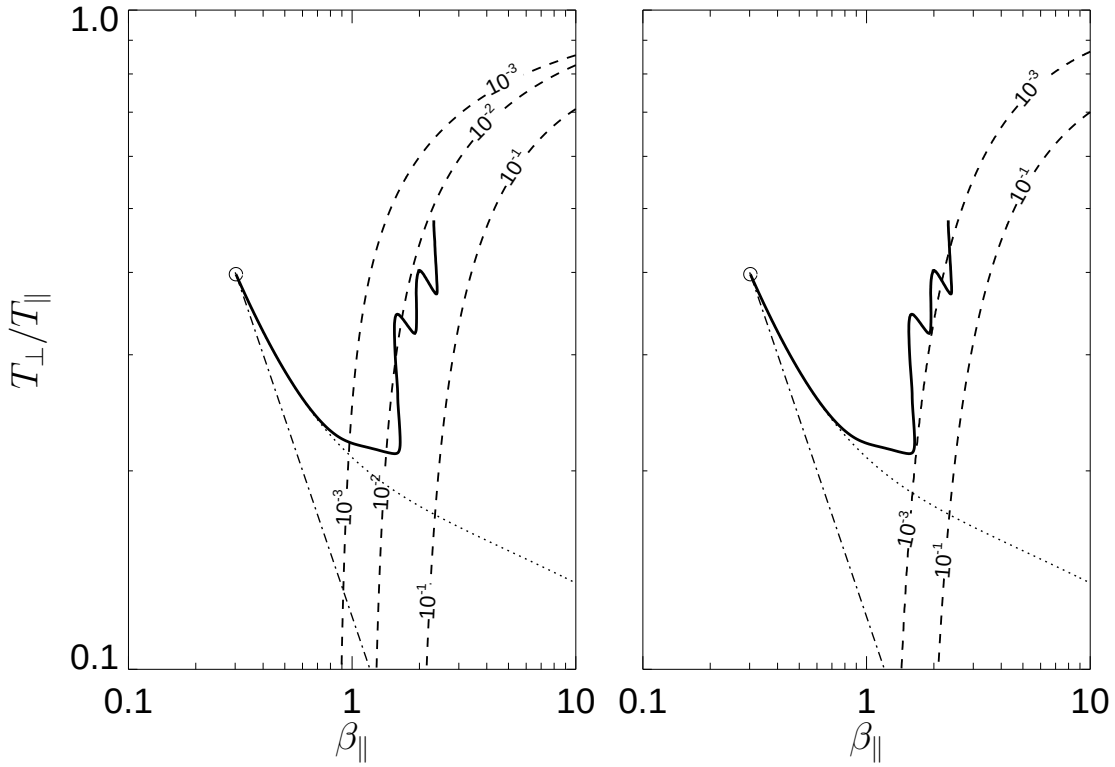

Figure 6: Evolution in the 2-D CHEB simulation: Path in the space $(\beta_\parallel, T_\perp/T_\parallel)$ is shown by solid curves; the empty circles denote the initial conditions whereas the full circles denotes the end of a first oscillation. The dashed contours shows the linear prediction in a homogeneous plasma with bi-Maxwellian protons, the maximum growth rate (in units of $\omega_{\rm cp}$) as a function of $\beta_\parallel$ and $T_\perp/T_\parallel$ for (left) the parallel proton fire hose and (right) the oblique one. The dotted lines display the collisional prediction whereas the dash-dotted lines show the collisionless, double adiabatic prediction.

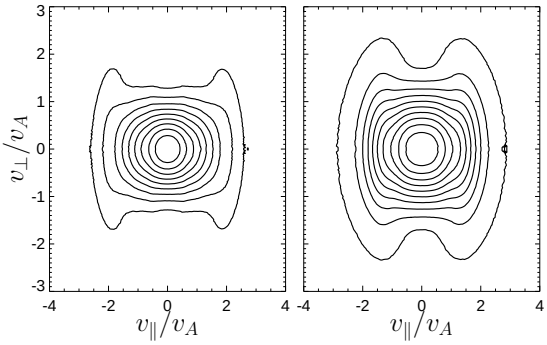

Figure 7: Contour plots of the proton distribution function $f(v_\parallel, v_\perp)$ at (left) $t = 0.4/\nu_{T0}$ and (right) at the and of the simulations.